Impact of random and periodic surface roughness on P- and L-band radiometry

Xiaoji Shen[a, *], Jeffrey P. Walker[a], Nan Ye[a], Xiaoling Wu[a], Foad Brakhasi[a], Nithyapriya Boopathi[a,b,c], Liujun Zhu[a,d], In-Young Yeo[e], Edward Kim[f], Yann Kerr[g], and Thomas Jackson[h]

[a]*Department of Civil Engineering, Monash University, Clayton, Australia*

[b]*Center of Studies in Resources Engineering, IIT Bombay, Mumbai, Maharashtra, India*

[c]*IITB-Monash Research Academy, Mumbai, India*

[d]*Yangtze Institute for Conservation and Development, Hohai University, Nanjing, China*

[e]*School of Engineering, The University of Newcastle, Callaghan, Australia*

[f]*NASA Goddard Space Flight Center, Greenbelt, USA*

[g]*Centre d'Etudes Spatiales de la Biosphère, Toulouse, France*

[h]*USDA ARS Hydrology and Remote Sensing Laboratory (Retired), Beltsville, USA*

Revision submitted to: Remote Sensing of Environment

Date: 18 October 2021

[*]*Corresponding author.*

E-mail addresses: xiaoji.shen@monash.edu, xiaoji.shen@foxmail.com (X. Shen).

Abstract:

L-band passive microwave remote sensing is currently considered a robust technique for global monitoring of soil moisture. However, soil roughness complicates the relationship between brightness temperature and soil moisture, with current soil moisture retrieval algorithms typically assuming a constant roughness parameter globally, leading to a potential degradation in retrieval accuracy. This current investigation established a tower-based experiment site in Victoria, Australia. P-band (~40-cm wavelength/0.75 GHz) was compared with L-band (~21-cm wavelength/1.41 GHz) over random and periodic soil surfaces to determine if there is an improvement in brightness temperature simulation and soil moisture retrieval accuracy for bare soil conditions, due to reduced roughness impact when using a longer wavelength. The results showed that P-band was less impacted by random and periodic roughness than L-band, evidenced by more comparable statistics across different roughness conditions. The roughness effect from smooth surfaces (e.g., 0.8-cm root-mean-square height and 11.1-cm correlation length) could be potentially ignored at both P- and L-band with satisfactory simulation and retrieval performance. However, for rougher soil (e.g., 1.6-cm root-mean-square height and 6.8-cm correlation length), the roughness impact needed to be accounted for at both P- and L-band, with P-band observations showing less impact than L-band. Moreover, a sinusoidal soil surface with 10-cm amplitude and 80-cm period substantially impacted the brightness temperature simulation and soil moisture retrieval at both P- and L-band, which could not be fully accounted for using the SMOS and SMAP default roughness parameters. However, when retrieving roughness parameters along with soil moisture, the ubRMSE at P-band over periodic soil was improved to a similar level (0.01-0.02 m^3/m^3) as that of smooth flat soil (0.01 m^3/m^3), while L-band showed higher ubRMSE over the periodic soil (0.03-0.04 m^3/m^3) than over smooth flat soil (0.01 m^3/m^3). Accordingly, periodic roughness effects were reduced by using observations at P-band.

Keywords: Soil roughness, row structure, soil moisture retrieval, P-band, passive microwave

1 Introduction

Soil moisture (SM) plays a key role in the earth's system since it impacts the water, energy and biogeochemical cycles, and subsequently climate-change projections (Seneviratne et al., 2010). L-band (~21-cm wavelength/1.4 GHz) passive microwave remote sensing has been widely accepted as a robust technique for soil moisture remote sensing due to its all-time/weather capability, direct relationship with soil moisture, relatively deep sensing depth (~ 5 cm), and being a protected band allocated exclusively for radio astronomy and earth observation use (Wigneron et al., 2017). Moreover, L-band has advantages in reducing the impact from soil surface roughness and the vegetation canopy compared to shorter wavelengths due to its relatively long wavelength (Ulaby et al., 1986).

The scientific community has made great efforts to improve soil moisture retrieval models at L-band over the past five decades based on ground (Blinn and Quade, 1972; Njoku and O'Neill, 1982; Wigneron et al., 2001; Cano et al., 2010; Schwank et al., 2012; Zheng et al., 2019) and airborne (Blanchard, 1972; Paloscia et al., 1993; Rosnay et al., 2006; Merlin et al., 2008; Panciera et al., 2008; Colliander et al., 2017; Ye et al., 2020a; Ye et al., 2020b; Zhao et al., 2020b) experiments. As a result of supporting evidence on capability and expected benefits in applications, the European Space Agency (ESA) launched the Soil Moisture and Ocean Salinity (SMOS) satellite (Kerr et al., 2010) in 2009 and the National Aeronautics and Space Administration (NASA) launched the Soil Moisture Active Passive (SMAP) satellite (Entekhabi et al., 2010) in 2015; both with L-band radiometers.

It is well known that soil roughness effects complicate the microwave emission and reduce the sensitivity of brightness temperature (TB) to soil moisture (Choudhury et al., 1979; Newton and Rouse, 1980; Newton et al., 1982; Njoku and O'Neill, 1982; Wang et al., 1983). The soil roughness effects are considered to result from a mixture of complex phenomena including 3-D soil spatial heterogeneities, volume scattering under dry soil conditions, and soil anisotropy, making it impractical to model the effects physically (Panciera et al., 2009; Wigneron et al., 2017). Accordingly, a tractable semi-empirical model (referred to as the HQN model) was proposed by Wang and Choudhury (1981) and further developed by Prigent et al. (2000) to simulate the roughness effects over flat soil exhibiting only random roughness. This model has been adopted in the baseline soil moisture retrieval algorithms of the SMOS (Kerr et al., 2017) and SMAP (O'Neill et al., 2015) missions.

According to the Fraunhofer criterion (Ulaby et al., 1982), a surface may be considered electromagnetically smooth in the microwave range if the root-mean-square (rms) of the surface height distribution (rms height; otherwise known as s) fulfills $s < \frac{\lambda}{32\cos(\theta)}$, where λ is the observation wavelength and θ is the incidence angle. This provides a theoretical basis that asserts observations at longer wavelength should be less affected by soil roughness than those at shorter wavelength. This has also been demonstrated by experiments (Blinn and Quade, 1972; Wang et al., 1983). Moreover, periodic (e.g., sinusoidal) row structures, a common type of soil tillage used for cultivation purposes, usually result in larger roughness impacts on radiometric observations compared to flat soil (Ulaby et al., 1986). However, as these experiments focused on L-band and higher frequencies, a demonstration of the impact at P-band is lacking.

The periodic soil surface consists of micro-scale random variations, i.e., random roughness, superimposed on a macro-scale one-dimensional surface undulation, i.e., periodic roughness (Ulaby et al., 1986; Gao, 2016). A common modeling approach is to simulate the micro-scale roughness and assume that the macro-scale roughness acts like topography by changing the local incidence angle of the micro-scale roughness (Wang et al., 1980; Ulaby et al., 2014; Neelam et al., 2020). Wang et al. (1980) were the first to model the emissivity over a periodic surface at varying azimuth. However, the model was found to overestimate the influence of the row structure (Promes et al., 1988). While Promes et al. (1988) concluded that the periodic structures can be ignored in most cases without notable error at L-band, this has been challenged by Zheng et al. (2012), who showed that row structures can lead to a retrieval error of up to 0.1 m^3/m^3. The results of Pham et al. (2005) also indicated that the azimuthal signal present in periodic row structures can lead to a retrieval error.

The current soil moisture retrieval algorithms of the SMOS and SMAP missions assume constant roughness parameters of the HQN model for different land cover types (Entekhabi et al., 2014; Kerr et al., 2017). Additionally, the impact of a periodic soil surface has not been considered in the SMOS and SMAP algorithms due to difficulties such as the lack of a global map for row structure, row height, and orientation, etc. Since these assumptions and simplifications impose errors on the soil moisture datasets (Peng et al., 2017), global soil moisture sensing could be improved by using P-band radiometry, if it can be proven that the roughness effects are reduced from those at L-band. Consequently, use of the HQN model to account for roughness at P-band (~40-cm wavelength/0.75 GHz), including periodic row structure, is tested in this paper. This follows from the work of Shen et al. (2021) which demonstrated an increased moisture retrieval depth at P- compared to L-band.

2 Data

A comprehensive tower-based experimental site was established at Cora Lynn, Melbourne, Australia (Fig. 1, see https://www.prism.monash.edu/) in October 2017 for exploring P-band radiometer soil moisture remote sensing. The field was 160 m × 160 m in size and divided into four quadrants (numbered as Q1 to Q4 from the northwest clockwise). A ten-meter-high tower

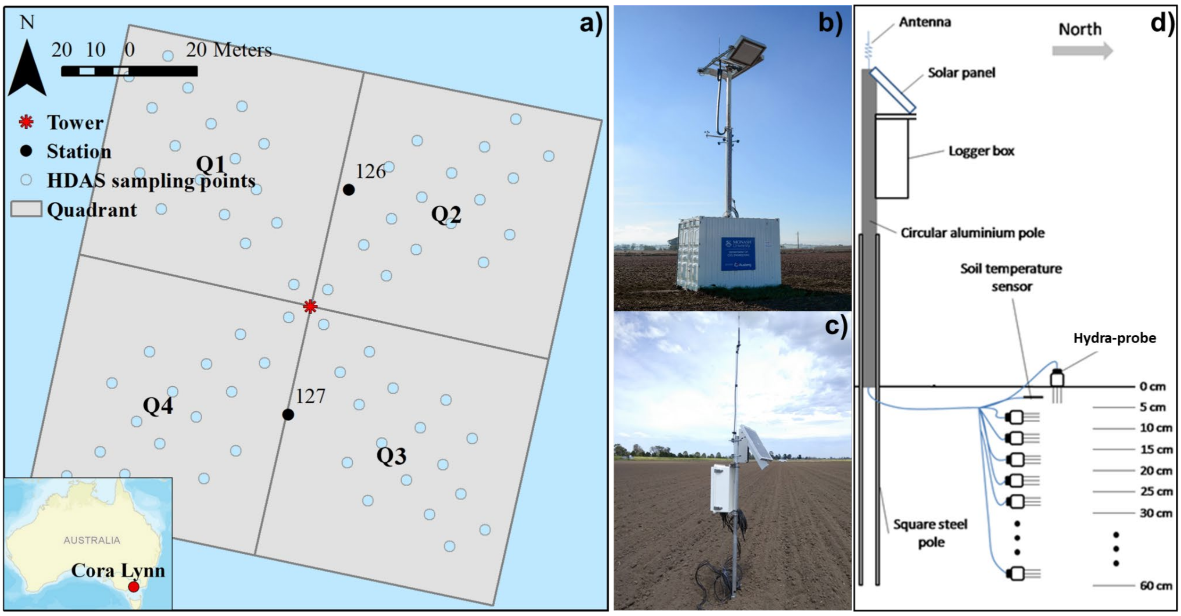

Fig. 1. Illustrations of the tower-based experiment at Cora Lynn, Melbourne, Australia, including a) location map of the site; b) the tower carrying PPMR and PLMR; c) a station monitoring soil moisture and temperature evolution; and d) diagram showing the installation of the stations.

was located at the center of the field, carrying the two radiometers (Fig. 1b), namely the Polarimetric P-band Multi-beam Radiometer (PPMR) and the Polarimetric L-band Multi-beam Radiometer (PLMR). The tower rotated and tilted the instruments on a schedule such that PPMR and PLMR alternatively observed the four quadrants of the paddock at a range of incidence angles. The spatial resolution of the 3-dB footprints of PPMR and PLMR for 40° incidence angle is approximately 8.2 m × 7.0 m and 4.0 m × 4.0 m, respectively.

The PPMR and PLMR operate at 0.742-0.752 GHz and 1.401-1.425 GHz, respectively. PPMR has four antenna beams at dual linear (horizontal (H) and vertical (V)) polarizations (H- and V-pol) while PLMR has six antenna beams at H- and V-pol. Warm and cold calibration of PPMR and PLMR were performed regularly: the former was undertaken weekly by positioning PPMR/PLMR over a blackbody chamber constructed from microwave absorbers and having 16 temperature sensors to provide the reference TB; the latter was performed every midnight according to the tower schedule by pointing the PPMR and PLMR towards the sky for 2 hours. The calibration accuracy for both the PPMR and PLMR was found to be better than 1.5 K. Note that the use of “P-band” and “L-band” hereafter specifically refers to the frequencies at which PPMR and PLMR operate unless otherwise specified.

For the period of data collection used in this paper, the temporal evolution of soil moisture and temperature was monitored by two stations (Fig. 1a, c) having 12 Hydra-probes inserted

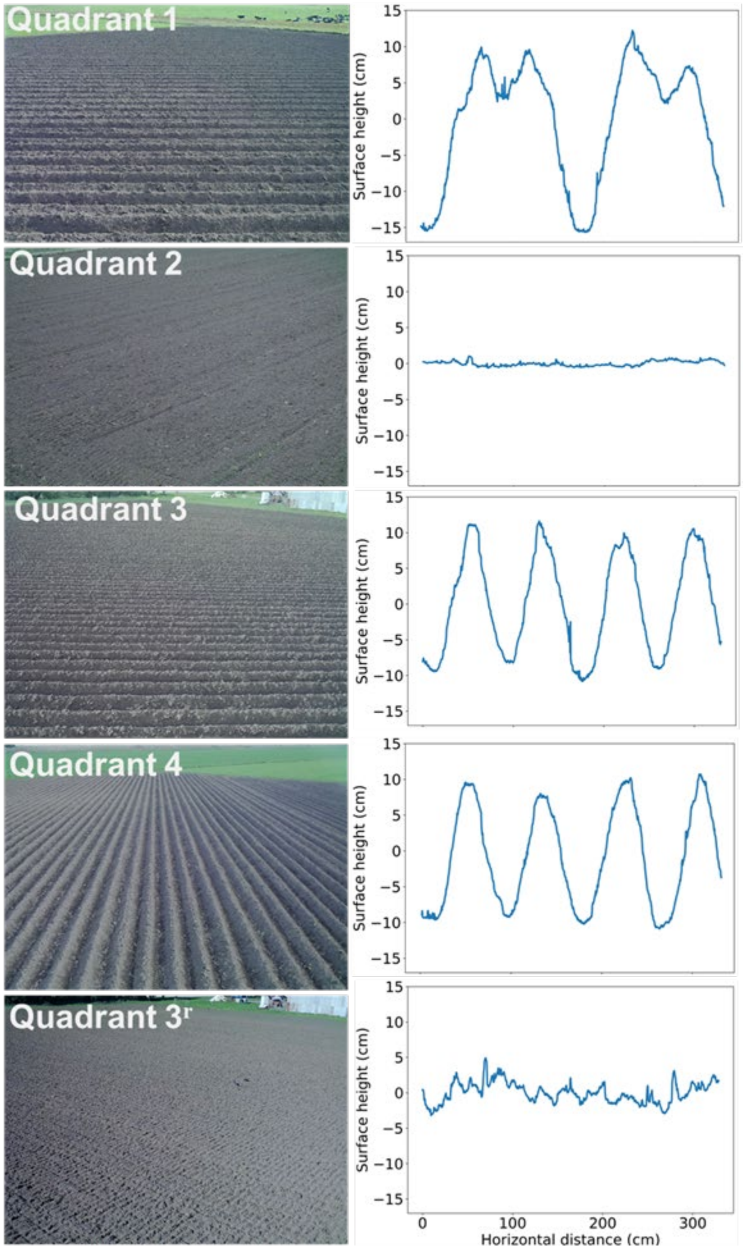

Fig. 2. Photos of the roughness conditions (left column) and soil profiles (right column) of the quadrants for the data used in this paper. Quadrants 3 and 4 were plowed in one pass and had the same roughness structures but with different orientations (perpendicular and parallel, respectively) relative to the tower look direction. Quadrant 3^{r} is quadrant 3 under a different roughness configuration.

into the soil at 5-cm increments down to 60 cm (Fig. 1d). To investigate the representativeness of the station, the spatial variation in surface soil moisture (~5 cm) was measured weekly at the locations shown in Fig. 1a using an in-house Hydra-probe Data Acquisition System (HDAS, Merlin et al., 2007). Particle size analysis on soil samples collected over the paddock found the soil to be a silt loam consisting of 18.0% clay, 10.9% sand, and 71.1% silt. The soil bulk density of the surface soil layer in this site was 0.87 kg/m^3.

The data collected from July 17, 2019 to July 31, 2019 were used in this paper. Because the field was plowed and sown with wheat in late July, only a limited period of data could be used for the study of bare soil. During this period, quadrants 1-4 were all bare soil and managed with different roughness conditions (Fig. 2, Table 1). Quadrant 2 was smooth flat soil while quadrants 1, 3, and 4 had periodic row structures. To provide a rougher flat bare soil as part of the comparison, the data in quadrant 3 collected from November 18, 2020 to November 30, 2020 were also used, referred to as quadrant 3^r hereafter. The periodic row structures in

Table 1. Characterization of the roughness structures in the five quadrants.

Quadrant	Row structure	Periodic roughness			Random roughness		
		Azimuth (°)	Period (cm)	Amplitude (cm)	RMS height (cm)	Correlation length (cm)	RMS slope
1	Sinusoidal bench	90	165	12	1.3 ± 0.2	5.4 ± 1.9	0.3 ± 0.1
2	Flat	–	–	–	0.8 ± 0.3	11.1 ± 4.4	0.1 ± 0.1
3	Sinusoidal	90	80	10	1.1 ± 0.3	5.5 ± 1.3	0.2 ± 0.1
4	Sinusoidal	0					
3^r	Flat	–	–	–	1.6 ± 0.6	6.8 ± 2.2	0.2 ± 0.0

The measurements in Q1, Q3, and Q4 were decomposed into periodic and random components for calculating the periodic and random roughness statistics, respectively. Quadrants 3 and 4 were plowed in one pass and had the same roughness structure (just different orientations relative to the tower look direction), and therefore the measurements in these two quadrants were averaged.

quadrants 1, 3, and 4 had different shapes and/or azimuth, with azimuth defined here as the angle between the radiometer look direction and the row direction. The period of the row structure is defined as the row spacing, while the amplitude is half of the vertical distance between the bottom and the top of the row.

The roughness measurements were performed on July 17 and 31, 2019 for quadrants 1-4 and on November 19, 2020 for quadrant 3^r. Three consecutive 1-m measurements (i.e., 3-m in total) in two perpendicular directions were conducted in every quadrant on every sampling day using a pin-profiler with an ~0.5-cm pin interval. Photographs of the pin-profiler were taken during measurements, and the heights of the red pin tops in the photographs were derived from image processing, for calculating the rms height and correlation length (Table 1). RMS slope was also calculated to characterize the surface roughness, being rms height divided by correlation length. Although it has been suggested that a roughness profile longer than 10 m is required to guarantee a good precision (Oh and Kay, 1998; Baghdadi et al., 2000), such a long profile is not practical to measure in field experiments, and so a 3-m profile has been widely taken as a compromise (McNairn et al., 2014; Neelam et al., 2020; Ye et al., 2020a; Zhao et al., 2020b).

In total, four profiles were measured for each of the quadrants labeled 1-4, and two profiles were measured in quadrant 3^r. The measurements were performed across and along the rows for the periodic surfaces. The profiles measured across the rows were decomposed into random (micro-scale) and periodic (macro-scale) components (Fig. 3). The periodic components (in orange in Fig. 3) of the profiles in quadrant 1 as well as quadrants 3 and 4 were approximated

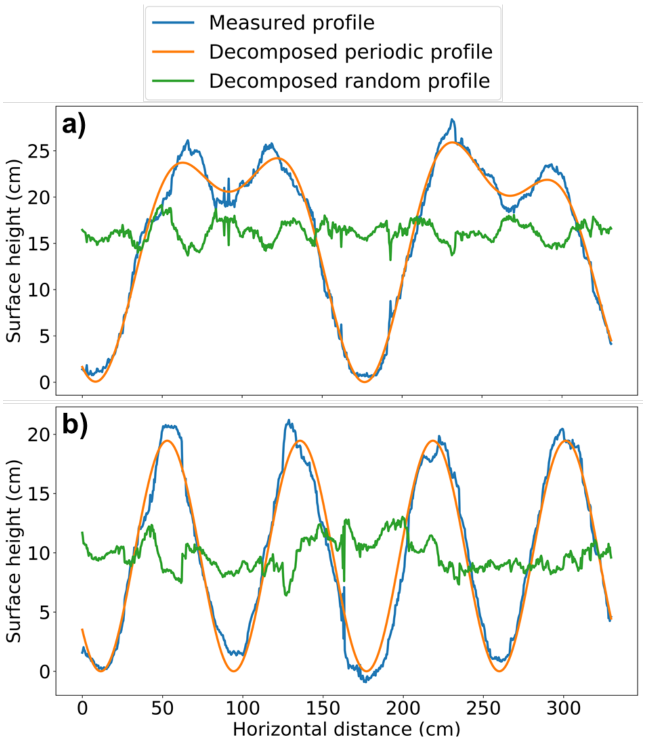

Fig. 3. Decomposition of measured roughness profile into periodic and random profiles, for a) the sinusoidal bench profile of quadrant 1 and b) the sinusoidal profile of quadrants 3 and 4.

using two-term and one-term sinusoidal functions, respectively. The fitting residuals (in green in Fig. 3) were taken as the random roughness component across the rows. The rms height, correlation length and rms slope in all five quadrants were calculated and averaged (with standard deviation) from using the random roughness components in the two perpendicular directions (Table 1). The roughness properties did not change much during the observing period, as indicated by the small standard deviation in Table 1, making it fair to assume a constant roughness condition over the analysis period. Consequently, the time-average of the rms height and correlation length measurements was used in this paper.

Fig. 4 presents the collected data during the study period. The TB data at 38° for L-band and 40° for P-band collected at around 6 am were plotted and used in this paper, with 6 am

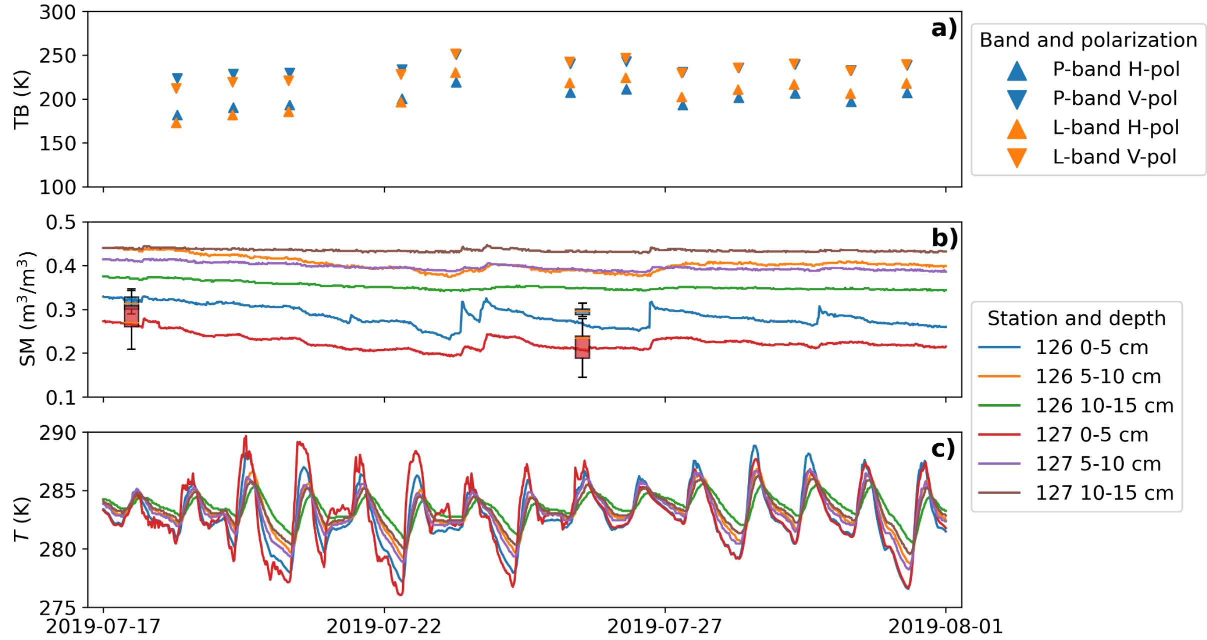

Fig. 4. Collected data including a) TB observations at 6 am in quadrant 1 as an example; b) station time-series soil moisture with weekly HDAS measurements (boxplots) on two occasions; and c) station time-series soil temperature. The data gaps in a) resulted from the tower being lowered due to high wind on those days. Only the data collected from the top 3 of the 12 sensors are plotted in b) and c). Corresponding to the soil moisture evolutions of station 126 (in blue) for quadrant 2 and station 127 (in red) for quadrants 1, 3, and 4, the HDAS measurements in quadrant 2, and quadrants 1, 3, and 4, are plotted as the blue and red boxplots in b), respectively, showing the maximum, 75% percentile, median, 25% percentile, and minimum.

used to minimize uncertainties from the soil temperature gradient and diurnal temperature variations (Fig. 4a). An approximately 40° incidence angle was used because 40° to 45° has been proven to provide the best retrieval accuracy (Zhao et al., 2020a) and 40° is also the incidence angle adopted by SMAP (Entekhabi et al., 2014).

The time series of soil moisture and temperature collected from stations 126 and 127 is plotted in Figs. 4b and c. Stations 126 and 127 showed similar soil moisture evolution over time, but with higher near-surface soil moisture values at station 126. The reason for this offset is that station 126 was in the flat quadrant, while station 127 was in the furrowed quadrant (Figs. 1a and 2); the drier moisture condition in the furrowed quadrants was also supported by the HDAS measurements shown in Fig. 4b. Considering the HDAS measurement agreement with the station soil moisture in the flat and periodic quadrants, in this paper station 126 was used as the soil moisture reference for quadrant 2 and station 127 was used as the soil moisture reference for quadrants 1, 3, and 4.

Consistent with the TB observations, the time-averaged soil moisture at around 6 am in the 0-5-cm layer was used to evaluate the retrieved soil moisture at P- and L-band. While the thermal sensing depth was calculated to be approximately 10 cm at L-band and 20 cm at P-band for a 0.3-m^3/m^3 moisture condition (Njoku and Entekhabi, 1996), the moisture retrieval depth was much less, being approximately 5 cm or less at L-band (Escorihuela et al., 2010; Liu et al., 2012; Zheng et al., 2019) and up to 10 cm at P-band (Shen et al., 2021). However, Shen et al. (2021) showed that the moisture retrieval depth varies with moisture condition and profile shape, and thus differs from time to time. Consequently, the moisture retrieval depth for the conditions of this study was calculated using the moisture retrieval depth model from Shen et al. (2021), being approximately 4-5 cm at P-band and 2-3 cm at L-band. Given the difficulty to monitor soil moisture in a layer shallower than 5 cm, and that the soil moisture between neighboring layers is highly correlated, the soil moisture observation in the 0-5-cm layer has been used as the reference for both the P- and L-band retrievals in this paper.

3 Method

3.1 Physical model for random roughness

To estimate the impact of soil surface roughness, a physical model (Ulaby et al., 1982; Fung, 1994) was used to calculate soil emissivity based on Kirchhoff's reciprocity theorem such that

$$e_P = 1 - \Gamma_P = 1 - \Gamma_P^{\mathrm{non}} - \Gamma_P^{\mathrm{coh}}, \tag{1}$$

where Γ_P^{non} and Γ_P^{coh} are the noncoherent and coherent soil surface reflectivity, and subscript *P* denotes either H or V polarization. The Γ_P^{coh} can be calculated as

$$\Gamma_P^{\mathrm{coh}} = \Gamma_P^{*} \exp\{-[2ks\cos(\theta)]^2\}, \tag{2}$$

where k is the wave number, s is the rms height of the soil surface, and Γ_P^{*} is the specular reflectivity calculated from the Fresnel equation as a function of the relative soil dielectric constant ε_r ($\varepsilon_r = \varepsilon_r' - j\varepsilon_r''$) including real ($'$) and imaginary ($''$) parts

$$\Gamma_H^{*} = \left|\frac{\cos(\theta)-\sqrt{\varepsilon_r-\sin^2(\theta)}}{\cos(\theta)+\sqrt{\varepsilon_r-\sin^2(\theta)}}\right|^2 \tag{3}$$

$$\Gamma_V^{*} = \left|\frac{\varepsilon_r\cos(\theta)-\sqrt{\varepsilon_r-\sin^2(\theta)}}{\varepsilon_r\cos(\theta)+\sqrt{\varepsilon_r-\sin^2(\theta)}}\right|^2. \tag{4}$$

The Γ_P^{non} can be obtained by integrating the bistatic scattering coefficient σ^s over the upper hemisphere

$$\Gamma_H^{\mathrm{non}} = \frac{1}{4\pi\cos(\theta)}\int_0^{2\pi}\int_0^{\pi/2}[\sigma_{HH}^{s}(\theta,\phi,\theta_s,\phi_s) + \sigma_{HV}^{s}(\theta,\phi,\theta_s,\phi_s)]\sin(\theta_s)d\theta_s d\phi_s \tag{5}$$

$$\Gamma_V^{\mathrm{non}} = \frac{1}{4\pi\cos(\theta)} \int_0^{2\pi} \int_0^{\pi/2} [\sigma_{VV}^s(\theta, \phi, \theta_s, \phi_s) + \sigma_{VH}^s(\theta, \phi, \theta_s, \phi_s)] \sin(\theta_s) d\theta_s d\phi_s, \quad (6)$$

where θ and ϕ are the zenith and azimuth of the incident direction, respectively, while θ_s and ϕ_s are the zenith and azimuth of the scattering direction, respectively. Moreover, σ_{PQ}^s (subscripts P and Q denote either H and V or V and H polarizations) was modeled by the I^{2}EM (Improved Integral Equation Model, Fung et al., 2002), being a physical model that solves Maxwell's equations by accounting for the boundary conditions on a rough soil surface. The I^{2}EM was compared with another descendant of the IEM (Fung et al., 1992; Fung, 1994), i.e., the Advanced IEM (AIEM, Chen et al., 2003), by Wu et al. (2008), showing that the I^{2}EM performed equally to or even better than the AIEM for low frequencies and small roughness, which is the case in this research. In addition, the I^{2}EM has been used in similar simulations of the emissivity of soil surfaces (e.g., Ulaby et al. 2014).

The main equation of the I^{2}EM used in this research is

$$\sigma_{PQ}^s = S(\theta, \theta_s) \frac{k^2}{2} \exp[-s^2(k_z^2 + k_{sz}^2)] \sum_{n=1}^{\infty} s^{2n} \left| I_{PQ}^n \right|^2 \frac{W^{(n)}(k_{sx} - k_x,\ k_{sy} - k_y)}{n!}, \quad (7)$$

where $S(\theta, \theta_s)$ is the bistatic shadowing function, $k_x = k\sin(\theta)\cos(\phi)$, $k_y = k\sin(\theta)\sin(\phi)$, $k_z = k\cos(\theta)$, with k_{sx}, k_{sy}, k_{sz} similarly defined in terms of the scattering angles θ_s and ϕ_s, and $W^{(n)}$ is the Fourier transform of the n^{th} power of the surface correlation coefficient. The inputs to the I^{2}EM are dielectric constant, observation frequency and surface properties including the type of correlation function, rms height and correlation length. An exponential correlation function was assumed in this research since soil surfaces are mostly considered exponential-like (Fung and Kuo, 2006; Schwank et al., 2009; Zhu et al., 2020).

The dielectric constant was related to soil moisture in this paper using the model of Mironov et al. (2013), because it accounts for the interfacial (Maxwell-Wagner) relaxation of water in the soil, which is important at P-band (Mironov et al., 2013). The Mironov model neglects the dependence of temperature on the dielectric constant by assuming a constant temperature of 20 °C. While the Peplinski model is also applicable at P-band (Peplinski et al., 1995), it was proven to have a much larger standard deviation from dielectric measurements (~0.3 compared to 0.014 using the Mironov model) and thus not adopted here (Mironov et al., 2013).

3.2 Physical model for sinusoidal surface

A one-dimensional sinusoidal surface with height $Z(y)$ can be described by

$$Z(y) = \mathrm{A}\left[1 + \cos\left(\frac{2\pi y}{\Lambda}\right)\right], \tag{8}$$

with amplitude A and spatial period Λ. Assuming that there are many spatial periods Λ within the antenna footprint, the emissivity of this sinusoidal surface ($e_P^{\sin}$) can be integrated across a single period such that (Ulaby et al., 2014)

$$e_P^{\sin}(\phi) = \frac{1}{\Lambda\cos(\theta)}\int_0^{\Lambda} e_P \sec(\alpha)\cos(\theta')\, dy, \tag{9}$$

where θ is the beam incidence angle, ϕ is the beam azimuth angle, e_P is the emissivity of the local small-scale surface with local incidence angle θ' calculated using Eq. 1, and α is the angle whose tangent is equal to the slope of the surface $Z(y)$. Please refer to Ulaby et al.

(2014) for more details on this model. Apart from the regular inputs of the I^{2}EM model, additional input requirements include azimuth, amplitude and period of the sinusoidal surface.

3.3 Semi-empirical model

This paper adopted the semi-empirical zero-order incoherent model (Ulaby et al., 1986) as the forward model to retrieve soil moisture from the tower brightness temperature observations. The total intensity of the thermal emission measured by radiometers (TB_P) is the sum of the brightness temperature from soil ($\mathrm{TB}_P^{\mathrm{s}}$) and the downwelling sky emission ($\mathrm{TB}^{\mathrm{sky\_down}}$) reflected by the soil ($\mathrm{TB}_P^{\mathrm{sky}}$)

$$\mathrm{TB}_P = \mathrm{TB}_P^{\mathrm{s}} + \mathrm{TB}_P^{\mathrm{sky}} = (1 - \Gamma_P)T_{\mathrm{eff}}^{\mathrm{s}} + \mathrm{TB}^{\mathrm{sky\_down}}\Gamma_P, \tag{10}$$

with Γ_P and $T_{\mathrm{eff}}^{\mathrm{s}}$ representing the reflectivity and effective temperature of the soil, respectively. The $\mathrm{TB}^{\mathrm{sky\_down}}$ was assumed to be constant and calculated to be 13.9 K at P-band and 5.3 K at L-band (ITU, 2015).

Kirchhoff's reciprocity theorem relates e_P to Γ_P through

$$e_P = 1 - \Gamma_P, \tag{11}$$

where Γ_P can be computed using the HQN model (Choudhury et al., 1979; Wang and Choudhury, 1981; Prigent et al., 2000)

$$\Gamma_P = \Gamma_P^{*}\exp[-H_R\cos^{N_{RP}}(\theta)] \tag{12}$$

for low frequencies, i.e., P- and L-band, with the Q_R parameter set to zero as it is commonly believed to be negligible (Wigneron et al., 2001; Wigneron et al., 2011; Lawrence et al., 2013).

The empirical parameters H_R and N_{RP} characterize the intensity of the roughness effects and polarization dependence, respectively. Γ_P^* is the specular reflectivity calculated by the Fresnel equations (Eqs. 3 and 4).

According to radiative transfer theory, $T_{\mathrm{eff}}^{\mathrm{s}}$ can be computed as (Choudhury et al., 1982)

$$T_{\mathrm{eff}}^{\mathrm{s}} = \int_0^\infty T(z)\alpha(z) \exp\left[-\int_0^z \alpha(z')dz'\right] dz, \tag{13}$$

where $T(z)$ is the soil temperature at depth z, and $\alpha(z)$ is the power absorption coefficient depending on the soil dielectric constant ε_r and the observation wavelength λ written as (Ulaby et al., 1986)

$$\alpha(z) = 2(2\pi/\lambda)\left|\mathrm{Im}\left[\sqrt{\varepsilon_r(z)}\right]\right|, \tag{14}$$

where Im[ ] represents the imaginary part. In this paper, the effective temperature was calculated using Eqs. 13 and 14 as well as the soil moisture and temperature measurements. The soil was modeled as a semi-infinite medium using the soil moisture and temperature observations from the twelve hydra-probes of the station, respectively, with the soil moisture and temperature below 60 cm assumed to be the same as those observed in the 55-60-cm layer.

Roughness has been found to impact microwave radiometry by reducing polarization difference, i.e., the depolarization effect (Shi et al., 2002; Mialon et al., 2012). Accordingly, the magnitude of the depolarization effect was calculated as

$$\Delta\Gamma = (\Gamma_H - \Gamma_V) - (\Gamma_H^* - \Gamma_V^*). \tag{15}$$

3.4 Inversion algorithm

In this paper the roughness parameters were retrieved together with the soil moisture as a single process, using the full-time series of P- and L-band observations (Fig. 4) over each quadrant individually, i.e., 24 observations at both H- and V-pol per band per quadrant were used to retrieve 15 unknowns (i.e., soil moisture across 12 days plus H_R, N_{RH}, N_{RV}). No calibration of these parameters was undertaken to ensure a fair comparison of the roughness impact for P- and L-band. With the assumption that the roughness remained constant over the study period, use of the full-time series of measurements allowed for a robust estimation of the retrieved roughness parameters, as they become less sensitive to measurement noise and/or small imperfections in the forward model (Konings et al., 2016).

Inversion of the forward model used a generalized least-squares iterative algorithm to minimize a cost function (CF) computed from the differences between observed ($\mathrm{TB}_P^{\mathrm{obs}}$) and simulated ($\mathrm{TB}_P$) TB, expressed as

$$\mathrm{CF} = \frac{\sum\left(\mathrm{TB}_P^{\mathrm{obs}} - \mathrm{TB}_P\right)^2}{\sigma(\mathrm{TB})^2} + \sum_i \frac{\left(P_i^{\mathrm{ini}} - P_i\right)^2}{\sigma(P_i)^2}, \tag{16}$$

where the sum of the difference between $\mathrm{TB}_P^{\mathrm{obs}}$ and TB_P was calculated using both polarizations at ~40° incidence angle during the retrieval period, $\sigma(\mathrm{TB})$ is the standard deviation related to the TB observations, P_i (i = 1, 2, 3, 4) is the value of the retrieved parameter (SM, H_R, N_{RH}, and N_{RV}), P_i^{ini} is the initial value of each retrieved parameter, and $\sigma(P_i)$ is the standard deviation associated with these initial values.

4 Results

4.1 Theoretical impact of random surface roughness

Fig. 5 shows the smooth surface roughness limit for different wavelengths and incidence angles according to the Fraunhofer criterion (Ulaby et al., 1982). Accordingly, it can be seen that at 40° incidence angle, the roughness effects can notionally be ignored at both P- and L-band providing the rms roughness height is lower than 0.8 cm. However, for a surface with rms height ranging from 0.8 to 1.6 cm it can only be considered electromagnetically smooth at P-band. Moreover, if the rms height increases beyond 1.6 cm, it suggests that the roughness cannot be neglected even at P-band.

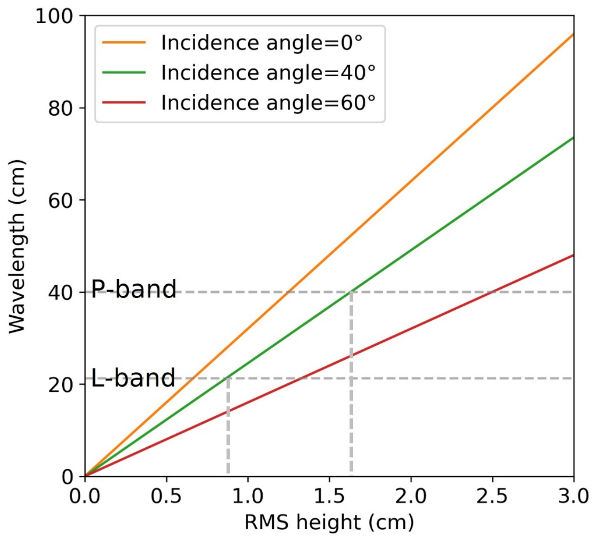

Fig. 5. The maximum rms height to consider a surface electromagnetically smooth for a given observation wavelength in the microwave range, calculated using the Fraunhofer criterion (Ulaby et al., 1982).

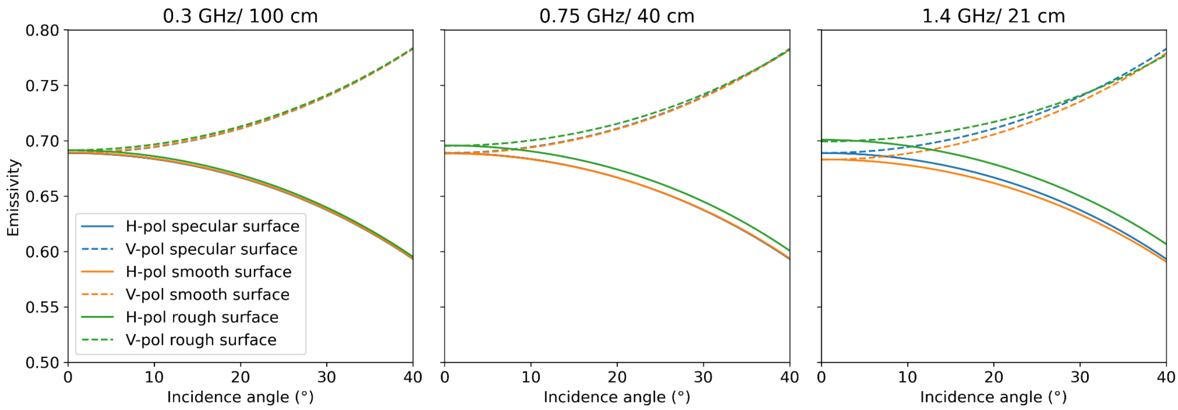

Fig. 6. Emissivity simulated using the physical model over different soil surfaces and at three frequencies, i.e., 0.3 GHz, 0.75 GHz, and 1.4 GHz. The dielectric constant was assumed to be 12 - *j*2.4 (~0.25 m^3/m^3 in soil moisture). The specular surface was assumed to have zero rms height and 50-cm correlation length. The rms height and correlation length of quadrants 2 and 3^r, being the break points according to the Fraunhofer criterion, were adopted in the simulation as the smooth and rough surface here, respectively.

Fig. 6 presents the simulated emissivity using the physical model (Eqs. 1-7) for a specular surface, a smooth surface with 0.8-cm rms height and 11.1-cm correlation length as observed in quadrant 2, and a relatively rough surface with 1.6-cm rms height and 6.8-cm correlation length as observed in quadrant 3^r, encompassing the roughness range of typical flat soil surfaces, being mostly located within the range of 0.5-2 cm and 4-15 cm for rms height and correlation length, respectively (Mialon et al., 2012; Lawrence et al., 2013; Fernandez-Moran et al., 2015). In Fig. 6, the offset from the specular surface curve can characterize the impact of the random roughness, being reduced at longer wavelengths. Accordingly, a surface with 0.8-cm rms height and 11.1-cm correlation length could be considered smooth at 0.3 GHz/100-cm wavelength and 0.75 GHz/40-cm wavelength, evidenced by the overlapped blue and orange curves. This also was true at 1.4 GHz/21-cm wavelength for incidence angles close to 40°. For the rough surface, the roughness effects could be ignored at 0.3 GHz/100-cm wavelength but not at 0.75 GHz/40-cm wavelength or 1.4 GHz/21-cm wavelength. However, it can still be seen that the impact at 1.4 GHz/21-cm wavelength was more pronounced than that at 0.75 GHz/40-cm wavelength.

4.2 Forward simulation using the Fresnel model

Fig. 7 shows the simulated against observed emissivity at both P- and L-band. From the comparison of P- and L-band emissivity in Fig. 7, it can be observed that overall P-band outperformed L-band in terms of both correlation coefficient (R) and unbiased root-mean-square error (ubRMSE), indicating that P-band observations were more representative to the 0-5-cm soil moisture compared to L-band observations. Due to the smoothness of quadrant 2, the scatter plots of quadrant 2 were very close to the 1:1 line for both P- and L-band. This demonstrates the possibility for the roughness impact of smooth soil surfaces, such as those in quadrant 2, to be limited at P- and L-band. However, the roughness impact was more

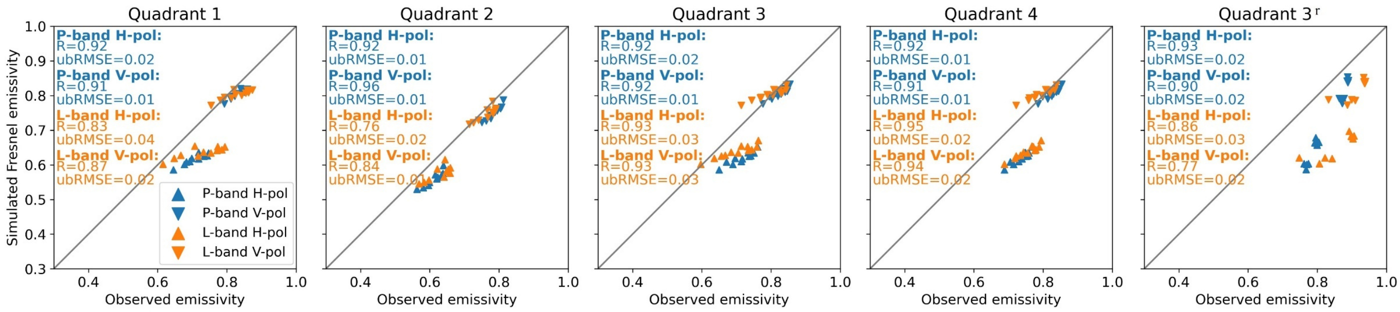

Fig. 7. Comparison of emissivity simulations using the Fresnel model against observations at P- and L-band.

considerable in the other four quadrants, having either periodic roughness or large random roughness. In addition, H-pol observations seemed to be influenced by roughness to a larger degree than V-pol observations, particularly in those quadrants with large roughness.

4.3 Physical simulation of multi-scale roughness

Fig. 8 shows the comparison of simulated and observed emissivity using the physical model over different periodic surfaces. Only sinusoidal surfaces (quadrants 3 and 4) were considered herein to explore the multi-roughness and azimuth issue. First, only the random roughness was modeled using the physical model (Eqs. 1-7) by ignoring periodic roughness. Next, the physical model for sinusoidal surfaces (Eqs. 1-9) was used to simulate the multi-scale roughness with random roughness on top of periodic roughness. The roughness measurements in Table 1 were used in simulations accordingly.

Similar to Fig. 7, it can be seen in Fig. 8 that P-band had a better performance than L-band in all scenarios. Although the ubRMSE in quadrant 3 was the same at P- and L-band, P-band had higher R values compared to L-band. From the comparison of top and bottom rows, the performance in quadrant 4 was improved substantially after accounting for the periodic roughness, while the statistics were degraded in quadrant 3. Notably, Promes et al. (1988) observed that another similar model (Wang et al., 1980) had a better agreement with observations for parallel- than perpendicular-look direction. Therefore, it is suggested that this type of model should be used with caution over periodic surfaces with a perpendicular-look direction.

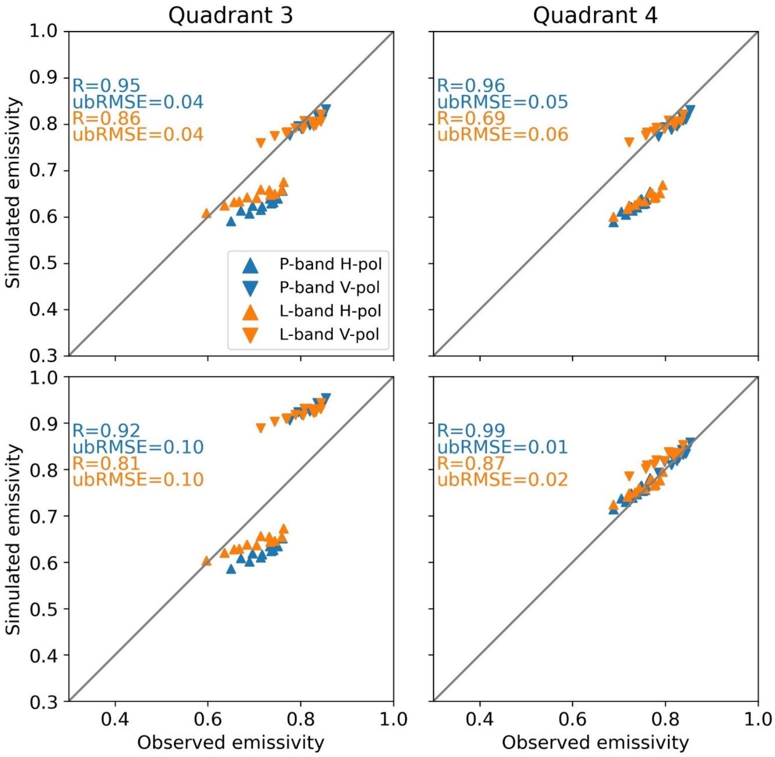

Fig. 8. Emissivity simulations compared against observations at P- and L-band using the physical model over sinusoidal surfaces. Top row: only random roughness was simulated; and bottom row: both periodic and random roughness was simulated.

4.4 Soil moisture retrieval using the semi-empirical model

Soil moisture retrieval was carried out using the semi-empirical model introduced in Section 3.3 through minimizing the cost function in Eq. 16. Table 2 presents the root-mean-square error (RMSE) for the four retrieval schemes in each quadrant. The initial values of all retrieved parameters were set to zero to avoid any potentially misleading prior knowledge in the retrieval (Wigneron et al., 2011). All four schemes made the retrieved SM and H_R "free" variables by omitting them from the cost function (Eq. 16).

Scheme 1 used the Fresnel model only and did not account for the roughness impact with the HQN model, with RMSE being similar at P- and L-band in quadrants 1 to 4 but not in quadrant 3^r. Schemes 2 and 3 used the HQN model and the same roughness parameters (H_R, N_{RH}, and N_{RV}) as SMOS (Kerr et al., 2017) and SMAP (O'Neill et al., 2015) for bare soil, respectively. These two schemes had a similar parameter configuration and therefore the same RMSE in all quadrants except quadrant 4 for L-band. The average accuracy of the five quadrants for schemes 2 and 3 was the same, being 0.03 m^3/m^3 and 0.04 m^3/m^3 at P- and L-band respectively. Scheme 4 was a 4-parameter retrieval that retrieved H_R, N_{RH}, and N_{RV} together with SM, achieving the best performance in terms of the average RMSE. Overall, P-band was found to have a 0.01- to 0.02-m^3/m^3 improvement over L-band when using the HQN

Table 2. RMSE (m^3/m^3) of the retrieved soil moisture using different retrieval schemes in each quadrant.

Scheme No.	Retrieval scheme	P-band						L-band					
		Q1	Q2	Q3	Q4	Q3^r	Avg	Q1	Q2	Q3	Q4	Q3^r	Avg
1	Retrieved parameter: SM σ(TB) = 0.5	0.05	0.03	0.05	0.06	0.05	0.05	0.06	0.03	0.04	0.05	0.08	0.05
2	Constant parameter: H_R = 0.1, N_{RH} = 2, N_{RV} = 0 Retrieved parameter: SM σ(TB) = 0.5	0.03	0.02	0.03	0.04	0.04	0.03	0.05	0.02	0.04	0.04	0.07	0.04
3	Constant parameter: H_R = 0.15, N_{RH} = N_{RV} = 2 Retrieved parameter: SM σ(TB) = 0.5	0.03	0.02	0.03	0.04	0.04	0.03	0.05	0.02	0.04	0.03	0.07	0.04
4	Retrieved parameter: SM, H_R, N_{RH}, N_{RV} σ(TB) = 0.5, $\sigma(N_{RP})$ = 5	0.02	0.02	0.02	0.02	0.03	0.02	0.04	0.02	0.04	0.05	0.04	0.04

Table 3. R and ubRMSE (m^3/m^3) of the retrieved SM using scheme 4 in each quadrant.

Metrics	P-band						L-band					
	Q1	Q2	Q3	Q4	Q3^r	Avg	Q1	Q2	Q3	Q4	Q3^r	Avg
R	0.92	0.94	0.92	0.92	0.93	0.93	0.86	0.81	0.94	0.95	0.82	0.88
ubRMSE	0.02	0.01	0.02	0.01	0.02	0.02	0.04	0.01	0.04	0.03	0.03	0.03

model, except for quadrant 2 where P- and L-band had the same RMSE, possibly due to the low roughness.

The R and ubRMSE were also computed for scheme 4 as an example and shown in Table 3. Similar to the RMSE results in Table 2, it can be observed that P-band still outperformed L-band in each quadrant. For quadrant 2 with a smooth soil surface, while the ubRMSE at P- and L-band was the same, the R value was higher at P-band. Compared to the ubRMSE in quadrant 2, the ubRMSE in other quadrants was similar at P-band while much higher at L-band.

Table 4 shows the roughness parameters retrieved simultaneously with soil moisture using scheme 4. Quadrant 2 had relatively low values of H_R and N_{RP}, indicating a minimal random roughness impact at P- and L-band. Compared to quadrant 2, the quadrants with periodic roughness (quadrants 1, 3 and 4) and the flat quadrant with higher roughness (quadrant 3^r) had a more substantial roughness impact on radiometric observations, evidenced by the larger H_R values and the larger difference between N_{RH} and N_{RV}.

Table 4. Retrieved roughness parameters in each quadrant using scheme 4.

Parameter	P-band					L-band				
	Q1	Q2	Q3	Q4	Q3^r	Q1	Q2	Q3	Q4	Q3^r
H_R	0.10	0.03	0.11	0.18	0.21	0.06	0.07	0.08	0.20	0.10
N_{RH}	-2.4	0	-2.9	-2.3	-1.9	-4.4	-1.6	-3.9	-3.5	-5.5
N_{RV}	2.4	0	3.0	2.4	2.0	4.4	1.6	4.0	3.5	5.6

Fig. 9 shows the magnitude of the depolarization effect of roughness (ΔΓ) using Eq. 15 and different N_{RP} values. It can be seen from the figure that both the SMOS (N_{RH} = 2 and N_{RV} = 0) and SMAP (N_{RH} = N_{RV} = 2) parameterization did not imply a substantial depolarization effect, being close to 0. Mapping the N_{RP} values in Table 4 to Fig. 9, it was found that P-band had a reduced depolarization compared to L-band, confirming the reduced roughness impact at P-band.

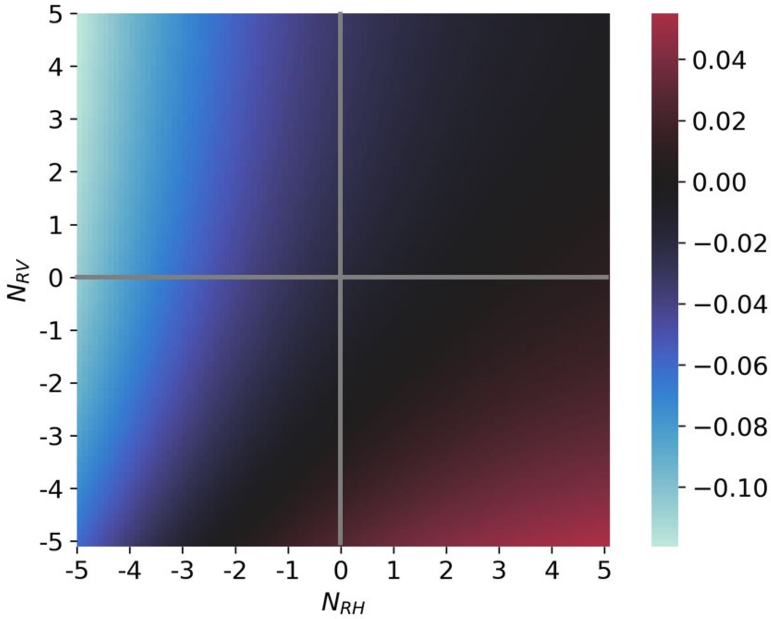

Fig. 9. Magnitude of the depolarization effect (ΔΓ) calculated using different N_{RH} and N_{RV} values. The dielectric constant, H_R and incidence angle were assumed to be 12 - *j*2.4 (~0.25 m^3/m^3 in soil moisture), 0.1 and 40°, respectively.

5 Discussion

5.1 Impact of random roughness

The Fraunhofer criterion (Fig. 5) and physical modeling (Fig. 6) indicated that brightness temperature observations at a longer wavelength should have a reduced impact from random roughness. The soil moisture retrieval (Tables 2 and 3) showed that the difference of the RMSE and ubRMSE in quadrants 2 and 3^r was reduced at P-band (0.01 m^3/m^3) compared to L-band (0.02 m^3/m^3). Therefore, it could be concluded that P-band had a reduced roughness impact over typical random roughness conditions.

The retrieval result using scheme 1 in Table 2 shows that the RMSE of both P- and L-band in quadrant 2 was 0.03 m^3/m^3, being smaller than the 0.04-m^3/m^3 target accuracy of SMOS and SMAP even though scheme 1 did not account for the roughness effect. By contrast, the RMSE of quadrant 3^r was 0.05 m^3/m^3 and 0.08 m^3/m^3 at P- and L-band respectively. This indicates that the roughness impact for smooth flat surfaces (quadrant 2) can be potentially ignored while the impact for rougher flat surfaces (quadrant 3^r) should not be neglected either at P- or L-band. This is confirmed by Fig. 7 where lower ubRMSEs (0.01-0.02 m^3/m^3) were found in quadrant 2, but higher ubRMSEs (0.02-0.03 m^3/m^3) were observed in quadrant 3^r.

5.2 Impact of periodic roughness

Compared with L-band, a reduced impact from periodic roughness was observed at P-band. From the retrieval result of schemes 2 and 3 in Table 2, it can be seen that using the SMOS and SMAP default roughness parameters resulted in a good performance in quadrant 2 at both P- and L-band (RMSE = 0.02 m^3/m^3), but the performance over periodic soil was not as good, being 0.03-0.04 m^3/m^3 at P-band and 0.04-0.05 m^3/m^3 at L-band. When retrieving roughness parameters along with soil moisture in scheme 4, the RMSE in quadrants 1, 3, and 4 for P-band was reduced to the same level as that for quadrant 2 at 0.02 m^3/m^3, while the RMSE for L-band was higher in quadrants 1, 3, and 4 (0.04-0.05 m^3/m^3) than in quadrant 2 (0.02 m^3/m^3). Similar differences can also be seen from the ubRMSE results in Table 3. In addition, it can be noticed from Table 2 that the RMSE for L-band in quadrant 4 was slightly higher using scheme 4 (0.05 m^3/m^3) compared to using schemes 2 and 3 (0.04 and 0.03 m^3/m^3, respectively), indicating that it is necessary to account for the impact of the periodic roughness as also shown in Fig. 8. However, this only happened at L-band, demonstrating that use of P-band can reduce the impact of periodic roughness. Although the quadrants with periodic surfaces also had larger random roughness than the flat quadrant, e.g., 1.1-cm rms height for quadrants 3 and 4 and 0.8-cm rms height for quadrant 2 (Table 1), this should not vitiate the stated conclusion because the 0.3-cm difference could be ignored compared to the substantial periodic roughness influence, as shown in Fig. 8.

In terms of the retrieval performance (Tables 2 and 3) and the retrieved roughness parameters (Table 4), quadrant 1 (sinusoidal bench and perpendicularly oriented) was found to behave similarly to quadrant 3 (sinusoidal and perpendicularly oriented). Importantly, the orientation of the row structure mattered; while the retrieval performance was not substantially different between quadrants 3 and 4 (Table 3), the parallel row structure in quadrant 4 led to a larger H_R value and lower absolute value of N_{RP} (Table 4), in spite of the same row spacing and height. It should be noted that, although it fits with intuition that parallel row structures impose less roughness impact than perpendicular row structures, this is not the case according to either this research or the literature (Wang et al., 1980; Ulaby et al., 2014).

Although there have been a few models for simulating surfaces with multi-scale roughness (Wang et al., 1980; Ulaby et al., 2014), it is still impractical to use them in global soil moisture retrieval. Reasons include, 1) these models rely heavily on accurate roughness measurements including period, amplitude, and azimuth of the row structures which are difficult to obtain globally; and 2) the model accuracy was not always satisfactory (e.g., Fig. 8) even though the roughness measurements were carefully sampled in the field. This finding is supported by Promes et al. (1988) who evaluated the model from Wang et al. (1980) using ground-based observations and found this model tended to overestimate the influence of the row structure. A potential reason to explain this is that these models were developed based on some assumptions, e.g., the radiometer footprint contains many spatial periods, which may not be fulfilled when the footprint extends across only a few meters in ground-based experiments.

The current SMOS and SMAP algorithm does not specifically consider any correction of this periodic roughness effect. Reasons in addition to the difficulties noted earlier include that a mixture of flat soil and/or periodic soil structures with different orientations are often present in a large footprint, potentially averaging those effects. Nonetheless, this paper has demonstrated that P-band can achieve a higher retrieval accuracy than L-band when utilizing the current SMOS and SMAP algorithm over periodic surfaces.

5.3 Depolarization effects

The depolarization is due to the fact that roughness impacts amplify H-pol emissivity to a greater degree compared to V-pol emissivity (Shi et al., 2002; Mialon et al., 2012), in line with Figs. 6 and 7. This results in a reduced difference between H- and V-pol observations. In the mono-angular retrieval of this paper, N_{RP} can be seen as a coefficient of H_R that characterizes the intensity of roughness. A larger N_{RP} value makes the roughness coefficient, i.e., $\exp[-H_R \cos^{N_{RP}}(\theta)]$ in Eq. 12, closer to one, indicating a reduced roughness impact. Accordingly, ΔN_R, i.e., $\Delta N_R = N_{RH} - N_{RV}$, is able to characterize the depolarization effect.

Although N_{RH} and N_{RV} values differ from case to case, non-negative ΔN_R values have been often reported in the literature (Mialon et al., 2012; Lawrence et al., 2013) and used in the SMOS and SMAP retrieval algorithms (O'Neill et al., 2015; Kerr et al., 2017). However, in Table 4 negative ΔN_R values were obtained, possibly due to a substantial depolarization induced by the large roughness impact, particularly in quadrants 1, 3, 4 and 3^r. Moreover, the different retrieval configuration adopted in this paper could be another explanation. The multi-angular configuration adopted by Mialon et al. (2012) possibly imposed more constraints on N_{RP}, leading to a different result. However, a negative relation of ΔN_R and roughness was established by Mialon et al. (2012) and Lawrence et al. (2013), suggesting that ΔN_R could also become negative as roughness increases. Accordingly, negative ΔN_R was also seen by a few studies (Montpetit et al., 2015; Peng et al., 2017), in accordance with the current investigation.

Depolarization could adversely impact soil moisture retrieval. Konings et al. (2015) pointed out that a robust retrieval can only be guaranteed if the degree of information (DoI) of a set of observations is larger than the number of the retrieved parameters. Accordingly, this depolarization reduces the independence of the observations at H- and V-pol and thus the DoI. It can be noticed from Fig. 9 that $\Delta\Gamma$ is more likely to be non-positive, in line with literature observations that roughness-induced depolarization was often seen (Newton and Rouse, 1980; Wang et al., 1983; Mialon et al., 2012). A positive $\Delta\Gamma$ value is scarce to observe over bare soil because it indicates that roughness enlarges the difference between the reflectivity at both polarizations. This phenomenon can only be observed at low incidence angles (e.g., less than 20°) over periodic soil surfaces (Wang et al., 1980; Zheng et al., 2012). Consequently, N_{RP} values should be used with caution when ΔN_R is larger than 5, as indicated by the red area in Fig. 9.

5.4 Uncertainties

Although all results lend support to concluding that P-band is less sensitive to random and periodic roughness than L-band for the typical soil roughness landscapes tested in this paper, it should be noted that the difference in RMSE between P- and L-band could also be attributed to the potential error from using a mismatched moisture retrieval depth. The compromise of the evaluation in this paper is using the 5-cm moisture observation to evaluate the retrieved soil moisture of around 0-4/5 cm at P-band and 0-2/3 cm at L-band, due to the difficulty in measuring the soil moisture evolution of the top few centimeters. While it is possible to model the soil moisture at these depths, reliance on model estimates will bring further uncertainties and make the results somewhat unreliable.

To mitigate this issue, ubRMSE was also calculated since it removes the systematic error induced from the mismatched moisture depth. However, there may also be random errors imposed on the RMSE that cannot be removed by calculating ubRMSE. Accordingly, the reduced roughness impact of P-band was demonstrated in this paper by comparing the statistics in rough surfaces to those in flat surfaces instead of directly comparing the statistics of P- and L-band.

While L-band was found in some cases to have shallower moisture retrieval depth than the widely accepted 5 cm (Escorihuela et al., 2010; Zheng et al., 2019; Shen et al., 2021), most studies are still using the soil moisture observations at around 5 cm to validate soil moisture products (Zeng et al., 2015) and calibrate the HQN model parameters (Mialon et al., 2012). This potentially leads to a dependence of the calibrated roughness parameters on soil moisture, which has been found to be reduced by using the soil moisture at a shallower moisture retrieval depth (Escorihuela et al., 2010). From this perspective, the retrieval error caused by the mismatched moisture depth in this paper can be taken as the “effective” roughness impact if a 5-cm moisture retrieval depth is assumed at both P- and L-band.

The Fraunhofer criterion and the I^{2}EM also have limitations that might lead to some uncertainties in the results. The Fraunhofer criterion considers only the vertical roughness (i.e., rms height) by assuming a considerably larger period of the soil structures than the observation wavelength. In addition, the isotropic roughness properties assumed by the I^{2}EM may sometimes be invalid in practice.

6 Conclusion

This paper compared random and periodic roughness impacts on P- and L-band passive microwave brightness temperature to demonstrate the potential improvement in soil moisture retrieval from using the longer wavelength P-band observations rather than the shorter L-band observations over smooth to relatively rough soil. P-band was found to be less impacted by random and periodic roughness than L-band, evidenced by more comparable statistics across different roughness conditions. An important result is that the roughness impact for smooth flat surfaces (e.g., quadrant 2 with 0.8-cm rms height and 11.1-cm correlation length) can be ignored, and still provide a satisfactory retrieval performance at both P- and L-band. However, the impact of roughness became important when the rms height reached 1.6 cm with a correlation length of 6.8 cm (quadrant 3^r) at both P- and L-band, with P-band observations showing less impact than L-band.

Periodic roughness was seen to degrade the retrieval performance from flat surfaces and could not be fully accounted for using the SMOS and SMAP default roughness parameters. However, when retrieving roughness parameters along with soil moisture, the ubRMSE at P-band over periodic soil surfaces was improved to a similar level (0.01-0.02 m^3/m^3) of that for a flat soil (0.01 m^3/m^3), while L-band showed a higher ubRMSE over periodic soil surfaces

(0.03-0.04 m^3/m^3) than that over flat soil surfaces (0.01 m^3/m^3). This indicates reduced periodic surface roughness effects at P- compared to L-band.

Acknowledgment

This work was supported by the Australian Research Council through the Towards P-Band Soil Moisture Sensing from Space Project under Discovery Grant DP170102373, and Linkage, Infrastructure, Equipment and Facility Grants LE0453434 and LE150100047. This work was supported in part by the China Scholarship Council, IITB-Monash Research Academy, and Monash University. The authors wish to thank Pascal Mater and Kiri Mason for their help with maintenance of the experimental equipment and site. Thanks also goes to Mr. Wayne Tymensen for providing the land of the experiment site. The authors thank the anonymous reviewers for providing insightful comments and suggestions to improve the manuscript.

References

Baghdadi, N., Paillou, P., Grandjean, G., Dubois, P., & Davidson, M. (2000). Relationship between profile length and roughness variables for natural surfaces. *International Journal of Remote Sensing, 21*, 3375-3381

Blanchard, B.J. (1972). Measurements from aircraft to characterize watersheds. In, *4th Annual Earth Resources Program Review*. NASA, Lyndon B. Johnson Space Center, Houston, Tex.

Blinn, J.C., & Quade, J.G. (1972). Microwave properties of geological materials: Studies of penetration depth and moisture effects. In, *4th Annual Earth Resources Program Review*. NASA, Lyndon B. Johnson Space Center, Houston, Tex.

Cano, A., Saleh, K., Wigneron, J.-P., Antolín, C., Balling, J.E., Kerr, Y.H., Kruszewski, A., Millán-Scheiding, C., Søbjærg, S.S., Skou, N., & López-Baeza, E. (2010). The SMOS Mediterranean Ecosystem L-Band characterisation EXperiment (MELBEX-I) over natural shrubs. *Remote Sensing of Environment, 114*, 844-853

Chen, K.-S., Wu, T.-D., Tsang, L., Li, Q., Shi, J., & Fung, A.K. (2003). Emission of rough surfaces calculated by the integral equation method with comparison to three-dimensional moment method simulations. *IEEE Transactions on Geoscience and Remote Sensing, 41*, 90-101

Choudhury, B.J., Schmugge, T.J., Chang, A., & Newton, R.W. (1979). Effect of surface roughness on the microwave emission from soils. *Journal of Geophysical Research: Oceans, 84*, 5699-5706

Choudhury, B.J., Schmugge, T.J., & Mo, T. (1982). A parameterization of effective soil temperature for microwave emission. *Journal of Geophysical Research Oceans, 87*, 1301–1304

Colliander, A., Cosh, M.H., Misra, S., Jackson, T.J., Crow, W.T., Chan, S., Bindlish, R., Chae, C., Holifield Collins, C., & Yueh, S.H. (2017). Validation and scaling of soil moisture in a semi-arid environment: SMAP validation experiment 2015 (SMAPVEX15). *Remote Sensing of Environment, 196*, 101-112

Entekhabi, D., Njoku, E.G., O'Neill, P.E., Kellogg, K.H., Crow, W.T., Edelstein, W.N., Entin, J.K., Goodman, S.D., Jackson, T.J., Johnson, J., Kimball, J., Piepmeier, J.R., Koster, R.D., Martin, N., McDonald, K.C., Moghaddam, M., Moran, S., Reichle, R., Shi, J.C., Spencer, M.W., Thurman, S.W., Tsang, L., & Van Zyl, J. (2010). The Soil Moisture Active Passive (SMAP) Mission. *Proceedings of the IEEE, 98*, 704-716

Entekhabi, D., Yueh, S., O'Neill, P.E., Kellogg, K.H., Allen, A., Bindlish, R., Brown, M., Chan, S., Colliander, A., & Crow, W.T. (2014). SMAP Handbook–Soil Moisture Active Passive: Mapping Soil Moisture and Freeze/Thaw from Space

Escorihuela, M.J., Chanzy, A., Wigneron, J.P., & Kerr, Y.H. (2010). Effective soil moisture sampling depth of L-band radiometry: A case study. *Remote Sensing of Environment, 114*, 995-1001

Fernandez-Moran, R., Wigneron, J.P., Lopez-Baeza, E., Al-Yaari, A., Coll-Pajaron, A., Mialon, A., Miernecki, M., Parrens, M., Salgado-Hernanz, P.M., & Schwank, M. (2015). Roughness and vegetation parameterizations at L-band for soil moisture retrievals over a vineyard field. *Remote Sensing of Environment, 170*, 269-279

Fung, A., & Kuo, N. (2006). Backscattering from multi-scale and exponentially correlated surfaces. *Journal of Electromagnetic Waves and Applications, 20*, 3-11

Fung, A.K. (1994). Microwave scattering and emission models and their applications

Fung, A.K., Li, Z., & Chen, K.S. (1992). Backscattering from a randomly rough dielectric surface. *IEEE Transaction on Geoscience & Remote Sensing, 30*, 356-369

Fung, A.K., Liu, W.Y., Chen, K.S., & Tsay, M.K. (2002). An Improved Iem Model for Bistatic Scattering From Rough Surfaces. *Journal of Electromagnetic Waves & Applications, 16*, 689-702

Gao, Y. (2016). Joint active passive microwave soil moisture retrieval. In: Monash University

ITU (2015). International Telecommunication Union recommendation: Radio noise. In: ITU-R P.372-12

Kerr, Y.H., Waldteufel, P., Richaume, P., Ferrazzoli, P., & Wigneron, J.P. (2017). Algorithm Theoretical Basis Document (ATBD) for the SMOS Level 2 Soil Moisture Processor Development Continuation Project v3.10. In (p. 132). https://earth.esa.int/documents/10174/1854519/SMOS_L2_SM_ATBD: SM-ESL (CBSA)

Kerr, Y.H., Waldteufel, P., Wigneron, J.-P., Delwart, S., Cabot, F., Boutin, J., Escorihuela, M.-J., Font, J., Reul, N., Gruhier, C., Juglea, S.E., Drinkwater, M.R., Hahne, A., Martin-Neira, M., & Mecklenburg, S. (2010). The SMOS Mission: New Tool for Monitoring Key Elements of the Global Water Cycle. *Proceedings of the IEEE, 98*, 666-687

Konings, A.G., McColl, K.A., Piles, M., & Entekhabi, D. (2015). How Many Parameters Can Be Maximally Estimated From a Set of Measurements? *IEEE Geoscience & Remote Sensing Letters, 12*, 1081-1085

Konings, A.G., Piles, M., Rötzer, K., Mccoll, K.A., Chan, S.K., & Entekhabi, D. (2016). Vegetation optical depth and scattering albedo retrieval using time series of dual-polarized L-band radiometer observations. *Remote Sensing of Environment, 172*, 178-189

Lawrence, H., Wigneron, J.P., Demontoux, F., Mialon, A., & Kerr, Y.H. (2013). Evaluating the Semiempirical H–Q Model Used to Calculate the L-Band Emissivity of a Rough Bare Soil. *IEEE Transactions on Geoscience & Remote Sensing, 51*, 4075-4084

Liu, P.-W., De Roo, R.D., England, A.W., & Judge, J. (2012). Impact of moisture distribution within the sensing depth on L-and C-band emission in sandy soils. *IEEE Journal of Selected Topics in Applied Earth Observations and Remote Sensing, 6*, 887-899

McNairn, H., Jackson, T.J., Wiseman, G., Bélair, S., Berg, A., Bullock, P., Colliander, A., Cosh, M.H., Kim, S.-B., & Magagi, R. (2014). The soil moisture active passive validation experiment 2012 (SMAPVEX12): Prelaunch calibration and validation of the SMAP soil moisture algorithms. *IEEE Transactions on Geoscience and Remote Sensing, 53*, 2784-2801

Merlin, O., Walker, J.P., Kalma, J.D., Kim, E.J., Hacker, J., Panciera, R., Young, R., Summerell, G., Hornbuckle, J., Hafeez, M., & Jackson, T. (2008). The NAFE'06 data set: Towards soil moisture retrieval at intermediate resolution. *Advances in Water Resources, 31*, 1444-1455

Merlin, O., Walker, J.P., Panciera, R., Young, R., Kalma, J.D., & Kim, E.J. (2007). Soil

Moisture Measurement in Heterogeneous Terrain. In, *Modsim International Congress on Modelling & Simulation Land Water & Environmental Management Integrated Systems for Sustainability* (pp. 2604-2610)

Mialon, A., Wigneron, J.P., Rosnay, P.D., Escorihuela, M.J., & Kerr, Y.H. (2012). Evaluating the L-MEB Model From Long-Term Microwave Measurements Over a Rough Field, SMOSREX 2006. *IEEE Transactions on Geoscience & Remote Sensing, 50*, 1458-1467

Mironov, V.L., Bobrov, P.P., & Fomin, S.V. (2013). Multirelaxation Generalized Refractive Mixing Dielectric Model of Moist Soils. *IEEE Geoscience & Remote Sensing Letters, 10*, 603-606

Montpetit, B., Royer, A., Wigneron, J.P., Chanzy, A., & Mialon, A. (2015). Evaluation of multi-frequency bare soil microwave reflectivity models. *Remote Sensing of Environment, 162*, 186-195

Neelam, M., Colliander, A., Mohanty, B.P., Cosh, M.H., Misra, S., & Jackson, T.J. (2020). Multiscale Surface Roughness for Improved Soil Moisture Estimation. *IEEE Transactions on Geoscience and Remote Sensing, 58*, 5264-5276

Newton, R.W., Black, Q.R., Makanvand, S., Blanchard, A.J., & Jean, B.R. (1982). Soil moisture information and thermal microwave emission. *IEEE Transactions on Geoscience and Remote Sensing*, 275-281

Newton, R.W., & Rouse, J.W. (1980). Microwave radiometer measurements of soil moisture content. *Antennas & Propagation IEEE Transactions on, 28*, 680 - 686

Njoku, E., & O'Neill, P. (1982). Multifrequency Microwave Radiometer Measurements of Soil Moisture. *Geoscience and Remote Sensing, IEEE Transactions on, 20*, 468-475

Njoku, E.G., & Entekhabi, D. (1996). Passive microwave remote sensing of soil moisture. *Journal of Hydrology, 184*, 101-129

O'Neill, P., Chan, S., Njoku, E., Jackson, T., & Bindlish, R. (2015). SMAP Algorithm Theoretical Basis Document (ATBD) Level 2 & 3 Soil Moisture (Passive) Data Products Revision B. In (p. 80). https://smap.jpl.nasa.gov/documents/: JPL

Oh, Y., & Kay, Y.C. (1998). Condition for precise measurement of soil surface roughness. *IEEE Transactions on Geoscience and Remote Sensing, 36*, 691-695

Paloscia, S., Pampaloni, P., Chiarantini, L., Coppo, P., Gagliani, S., & Luzi, G. (1993). Multifrequency passive microwave remote sensing of soil moisture and roughness. *International Journal of Remote Sensing, 14*, 467-483

Panciera, R., Walker, J.P., Kalma, J.D., Kim, E.J., Hacker, J.M., Merlin, O., Berger, M., & Skou, N. (2008). The NAFE'05/CoSMOS Data Set: Toward SMOS Soil Moisture Retrieval, Downscaling, and Assimilation. *IEEE Transactions on Geoscience and Remote Sensing, 46*, 736-745

Panciera, R., Walker, J.P., & Merlin, O. (2009). Improved understanding of soil surface roughness parameterization for L-band passive microwave soil moisture retrieval. *IEEE Geoscience and Remote Sensing Letters, 6*, 625-629

Peng, B., Zhao, T., Shi, J., Lu, H., Mialon, A., Kerr, Y.H., Liang, X., & Guan, K. (2017). Reappraisal of the roughness effect parameterization schemes for L-band radiometry over bare soil. *Remote Sensing of Environment, 199*, 63-77

Peplinski, N.R., Ulaby, F.T., & Dobson, M.C. (1995). Dielectric properties of soils in the 0.3-1.3-GHz range. *IEEE Transactions on Geoscience & Remote Sensing, 33*, 803-807

Pham, H., Kim, E.J., & England, A.W. (2005). An analytical calibration approach for microwave polarimetric radiometers. *IEEE Transactions on Geoscience and Remote Sensing, 43*, 2443-2451

Prigent, C., Wigneron, J.-P., Rossow, W.B., & Pardo-Carrion, J.R. (2000). Frequency and angular variations of land surface microwave emissivities: Can we estimate SSM/T and AMSU emissivities from SSM/I emissivities? *IEEE Transactions on Geoscience and Remote Sensing, 38*, 2373-2386

Promes, P.M., Jackson, T.J., & Neill, P.E.O. (1988). Significance of agricultural row structure on the microwave emissivity of soils. *IEEE Transactions on Geoscience and Remote Sensing, 26*, 580-589

Rosnay, P.D., Calvet, J.C., Kerr, Y., Wigneron, J.P., Lema?Tre, F.O., Escorihuela, M.J., Sabater, J.M.O., Saleh, K., Barrié, J.L., & Bouhours, G. (2006). SMOSREX: A long term field campaign experiment for soil moisture and land surface processes remote sensing. *Remote Sensing of Environment, 102*, 377-389

Schwank, M., Volksch, I., Wigneron, J.-P., Kerr, Y.H., Mialon, A., De Rosnay, P., & Matzler, C. (2009). Comparison of two bare-soil reflectivity models and validation with L-band radiometer measurements. *IEEE Transactions on Geoscience and Remote Sensing, 48*, 325-337

Schwank, M., Wigneron, J., Lopez-Baeza, E., Volksch, I., Matzler, C., & Kerr, Y.H. (2012). L-Band Radiative Properties of Vine Vegetation at the MELBEX III SMOS Cal/Val Site. *IEEE Transactions on Geoscience and Remote Sensing, 50*, 1587-1601

Seneviratne, S.I., Corti, T., Davin, E.L., Hirschi, M., Jaeger, E.B., Lehner, I., Orlowsky, B., & Teuling, A.J. (2010). Investigating soil moisture–climate interactions in a changing climate: A review. *Earth-Science Reviews, 99*, 125-161

Shen, X., Walker, J.P., Ye, N., Wu, X., Boopathi, N., Yeo, I.Y., Zhang, L., & Zhu, L. (2021). Soil Moisture Retrieval Depth of P- and L-Band Radiometry: Predictions and Observations. *IEEE Transactions on Geoscience and Remote Sensing, 59*, 6814-6822

Shi, J., Chen, K.S., Li, Q., & Jackson, T.J. (2002). A parameterized surface reflectivity model and estimation of bare-surface soil moisture with L-band radiometer. *IEEE Transactions on Geoscience & Remote Sensing, 40*, 2674-2686

Ulaby, F.T., Long, D.G., Blackwell, W.J., Elachi, C., Fung, A.K., Ruf, C., Sarabandi, K., Zebker, H.A., & Van Zyl, J. (2014). *Microwave radar and radiometric remote sensing*. University of Michigan Press Ann Arbor

Ulaby, F.T., Moore, R.K., & Fung, A.K. (1982). Microwave Remote Sensing Active and Passive-Volume II: Radar Remote Sensing and Surface Scattering and Enission Theory*, ii*

Ulaby, F.T., Moore, R.K., & Fung, A.K. (1986). Microwave Remote Sensing: Active and passive. Vol. III: From theory to applications. *Artech House Inc, 22*, 1223 - 1227

Wang, J.R., & Choudhury, B.J. (1981). Remote sensing of soil moisture content, over bare field at 1.4 GHz frequency. *Journal of Geophysical Research: Oceans, 86*, 5277-5282

Wang, J.R., Newton, R.W., & Rouse, J.W. (1980). Passive microwave remote sensing of soil moisture: The effect of tilled row structure. *IEEE Transactions on Geoscience and Remote Sensing*, 296-302

Wang, J.R., O'Neill, P.E., Jackson, T.J., & Engman, E.T. (1983). Multifrequency Measurements of the Effects of Soil Moisture, Soil Texture, And Surface Roughness. *IEEE Transactions on Geoscience & Remote Sensing, 21:1*, 44-51

Wigneron, J.P., Chanzy, A., Kerr, Y.H., Lawrence, H., Shi, J., Escorihuela, M.J., Mironov, V., Mialon, A., Demontoux, F., & Rosnay, P.D. (2011). Evaluating an Improved Parameterization of the Soil Emission in L-MEB. *IEEE Transactions on Geoscience & Remote Sensing, 49*, 1177-1189

Wigneron, J.P., Jackson, T.J., O'Neill, P., De Lannoy, G., de Rosnay, P., Walker, J.P., Ferrazzoli, P., Mironov, V., Bircher, S., Grant, J.P., Kurum, M., Schwank, M., Munoz-Sabater, J., Das, N., Royer, A., Al-Yaari, A., Al Bitar, A., Fernandez-Moran, R., Lawrence, H., Mialon, A., Parrens, M., Richaume, P., Delwart, S., & Kerr, Y. (2017). Modelling the passive microwave signature from land surfaces: A review of recent results and application to the L-band SMOS & SMAP soil moisture retrieval algorithms. *Remote Sensing of Environment, 192*, 238-262

Wigneron, J.P., Laguerre, L., & Kerr, Y.H. (2001). A simple parameterization of the L-band microwave emission from rough agricultural soils. *IEEE Transactions on Geoscience & Remote Sensing, 39*, 1697-1707

Wu, T.-D., Chen, K.-S., Shi, J., Lee, H.-W., & Fung, A.K. (2008). A study of an AIEM model for bistatic scattering from randomly rough surfaces. *IEEE Transactions on Geoscience and Remote Sensing, 46*, 2584-2598

Ye, N., Walker, J.P., Wu, X., Jeu, R.d., Gao, Y., Jackson, T.J., Jonard, F., Kim, E., Merlin, O., Pauwels, V.R.N., Renzullo, L.J., Rüdiger, C., Sabaghy, S., Hebel, C.v., Yueh, S.H., & Zhu, L. (2020a). The Soil Moisture Active Passive Experiments: Validation of the SMAP Products in Australia. *IEEE Transactions on Geoscience and Remote Sensing*, 1-18

Ye, N., Walker, J.P., Yeo, I., Jackson, T.J., Kerr, Y., Kim, E., McGrath, A., PopStefanija, I., Goodberlet, M., & Hills, J. (2020b). Toward P-Band Passive Microwave Sensing of Soil Moisture. *IEEE Geoscience and Remote Sensing Letters*, 1-5

Zeng, J.Y., Li, Z., Chen, Q., Bi, H.Y., Qiu, J.X., & Zou, P.F. (2015). Evaluation of remotely sensed and reanalysis soil moisture products over the Tibetan Plateau using in-situ observations. *Remote Sensing of Environment, 163*, 91-110

Zhao, T., Hu, L., Shi, J., Lü, H., Li, S., Fan, D., Wang, P., Geng, D., Kang, C.S., & Zhang, Z. (2020a). Soil moisture retrievals using L-band radiometry from variable angular ground-based and airborne observations. *Remote Sensing of Environment, 248*, 111958

Zhao, T., Shi, J., Lv, L., Xu, H., Chen, D., Cui, Q., Jackson, T., Yan, G., Jia, L., Chen, L., Zhao, K., Xingming, Z., Zhao, L., Zheng, C., Ji, D., Xiong, C., Wang, T., Li, R., Pan, J., & Zhang, Z. (2020b). Soil moisture experiment in the Luan River supporting new satellite mission opportunities. *Remote Sensing of Environment, 240*, 111680

Zheng, D., Li, X., Wang, X., Wang, Z., Wen, J., van der Velde, R., Schwank, M., & Su, Z. (2019). Sampling depth of L-band radiometer measurements of soil moisture and freeze-thaw dynamics on the Tibetan Plateau. *Remote Sensing of Environment, 226*, 16-25

Zheng, X., Zhao, K., & Zhang, S. (2012). Results of soil moisture inversion from radiometer biased by periodic change of row structure on farmland. *Yaogan Xuebao- Journal of Remote Sensing, 16*, 1310-1230

Zhu, L., Walker, J.P., & Shen, X. (2020). Stochastic ensemble methods for multi-SAR-mission soil moisture retrieval. *Remote Sensing of Environment, 251*, 112099